Check for updates

Robust engineered catalyst for the conversion of brown grease to renewable diesel *via* decarboxylation/decarbonylation†

Great C. Umenweke,[ab] Brian Hogston,[a] Olivier Heintz,[c] Gilles Caboche,[c] Robert B. Pace[a] and Eduardo Santillan-Jimenez [ID] *[ab]

A novel engineered Ni–Cu/Al₂O₃ decarboxylation/decarbonylation catalyst achieved quantitative conversion of brown grease, excellent yield of diesel-like hydrocarbons, effective heteroatom removal, and remarkable resistance to deactivation for hundreds of hours on stream. This offers an industrial alternative to hydrotreating for transforming waste oleaginous feedstocks into renewable diesel and sustainable aviation fuel.

Alumina (γ-Al₂O₃) is extensively utilized as a catalyst support due to its mechanical strength, thermal stability, and high surface area, which helps enhance supported metal dispersion.[1] Catalysts comprising Ni supported on γ-Al₂O₃ find applications in reactions such as steam methane reforming[2] and propane dehydrogenation,[3] as well as in deoxygenation reactions such as hydrodeoxygenation (HDO)[4] and decarboxylation/decarbonylation (deCO$_x$).[5,6] Both monometallic and bimetallic formulations based on Ni supported on γ-Al₂O₃ can deoxygenate oleaginous biomass in the form of fats, oils, and greases (FOG) very effectively.[7] Particularly promising results have been obtained over Cu-promoted Ni/Al₂O₃ catalysts since Cu can simultaneously enhance the deoxygenation performance as well as curb the cracking activity and the coke-induced deactivation of Ni.[8,9] Despite the auspicious nature of the aforementioned results, most work to date has been performed using Ni–Cu/Al₂O₃ catalysts in their powder or pelletized form, batch or semi-batch reactors, and/or relatively short times on stream when continuous fixed-bed reactors have been employed.[1,6] Moreover, most studies to date have involved model compounds or triglyceride-based feedstocks low in contaminants as the feed. All this limits the relevance of the resulting data to larger-scale

industrial applications. Consequently, an engineered 20%Ni–5%Cu/Al₂O₃ (E-NCA) catalyst was synthesized, characterized, and tested in the conversion of brown grease (BG) – a waste feed consisting solely of free fatty acids (see Table S1, ESI†) that is currently unutilized as it is typically incinerated or landfilled – to renewable diesel (RD) for hundreds of hours on stream.

E-NCA was prepared *via* impregnation using Ni and Cu nitrates as the metal precursors and cylindrical shape γ-Al₂O₃ extrudates of 3.18 mm in size with a surface area (SA) of 221 m² g⁻¹ as the support. The textural properties of the resulting E-NCA catalyst, which was determined to have a bulk density of 0.76 g cm⁻³, were measured *via* N₂ physisorption to afford the results in Table 1. Unsurprisingly, E-NCA possesses a lower surface area relative to the bare support due to the partial blockage of pore channels by metal particles. Parenthetically, H₂ pulse chemisorption was used to measure the Ni-specific surface area, which was determined to be 2.77 m² g⁻¹. The metal loading of E-NCA was measured by means of inductively coupled plasma-mass spectrometry (ICP-MS) and confirmed to be very close to the nominal values (see Table 1). The E-NCA catalyst was also analyzed by means of x-ray diffraction (XRD) to obtain the diffractogram in Fig. S1 (ESI†). In addition to diffraction peaks corresponding to γ-Al₂O₃, diffraction peaks at 37.2°, 43.3°, and 62.9° respectively attributed to the (1 1 1), (2 0 0), and (2 2 2) facets of NiO were observed. By applying the Scherrer equation to the peak at 37.2° an average NiO particle size of 4.4 nm was calculated.

The E-NCA catalyst was also characterized *via* transmission electron microscopy-energy dispersive spectroscopy (TEM-EDS) to afford the results summarized in Fig. 1 as well as in Fig. S2(a) and S2(b) (ESI†). The metal particle size distribution of E-NCA shown in Fig. 1(a) ranges from 2 to 22 nm, with an average particle size of 8.5 ± 3.8 nm, which is in overall agreement with

[a] *University of Kentucky Center for Applied Energy Research, Lexington, KY 40511, USA*

[b] *University of Kentucky Department of Chemistry, Lexington, KY 40506, USA. E-mail: esant3@uky.edu*

[c] *Université Bourgogne Europe, CNRS, Laboratoire Interdisciplinaire Carnot de Bourgogne ICB UMR 6303, 21000 Dijon, France*

† Electronic supplementary information (ESI) available. See DOI: https://doi.org/10.1039/d5cc01451d

Table 1 E-NCA textural properties, metal loading, and particle size

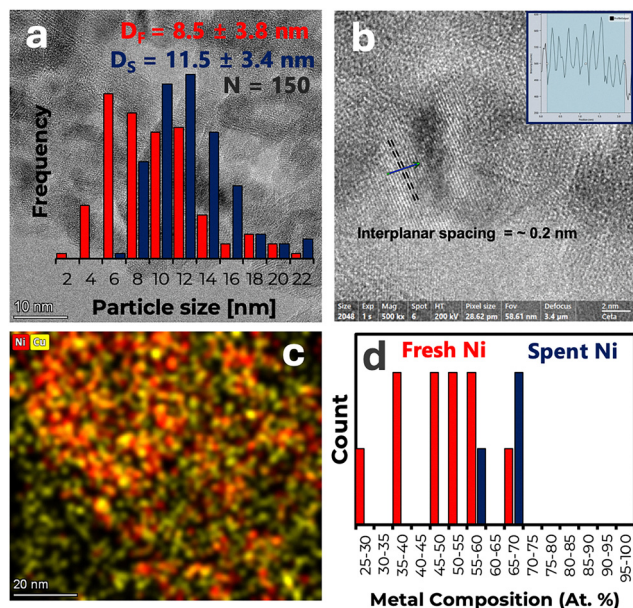|	SA (m² g⁻¹)	Pore vol. (cm³ g⁻¹)	Pore size (nm)	Ni (%)	Cu (%)	NiO crystallite size (nm)
E-NCA	140.8	0.39	11.0	19.5	5.6	4.4

Fig. 1 (a) Particle size distribution; (b) interplanar spacing of (1 1 1) plane; (c) elemental maps; (d) Ni content.

the value calculated *via* XRD. The high-resolution TEM image in Fig. 1(b) shows an interplanar d-spacing of ~ 0.2 nm, which is the value reported for the (1 1 1) plane of both Ni and Cu.[10,11] The crystalline nature of the metal particles within E-NCA is also confirmed by the fast Fourier transform (FFT) image inset in Fig. S2(a) in the ESI.† The STEM-High-angle annular dark-field imaging (HAADF) micrograph for E-NCA and the corresponding elemental maps of Ni and Cu are displayed in Fig. S2(b) in the ESI† and in Fig. 1(c), respectively, elemental maps of Al and O also being included in Fig. S3 (ESI†). Notably, albeit both Ni and Cu are uniformly distributed on the support and all Ni appears to be associated with Cu, some Cu is detected in regions where Ni is less abundant or absent altogether (see bottom left corner of Fig. 1(c)). The composition of individual metal particles was also determined by means of TEM-EDS. Ni content was observed to range from 25 to 70%, albeit most particles had a Ni content between 45 and 60% (see Fig. 1(d)). This observation, which is admittedly based on a limited sample, confirms that all Ni is associated with Cu (and/or other elements like Al and O).

Temperature-programmed studies were performed on E-NCA to assess both catalyst acidity and reducibility. Fig. S2(c) in the ESI† shows the trace associated with the temperature-programmed desorption (TPD) of ammonia, which revealed that E-NCA contains acid sites of various strengths. Weakly acidic sites displaying the lowest NH_3 desorption temperatures (<400 °C) are the least abundant, while sites of medium acidity (from which NH_3 desorbs between 400 and 650 °C) are the most abundant. Strongly acidic sites displaying the highest NH_3 desorption temperatures (>650 °C) – and mainly attributed to Lewis acid sites[12] – were also observed to be fairly abundant. Fig. S2(d) in the ESI† shows the trace associated with the temperature-programmed reduction (TPR) of E-NCA, which includes four main reduction events. The sharp peak at 200 °C is attributed to CuO

reduction to metallic Cu, while the peak with a maximum at 380 °C represents the reduction of a NiO–CuO phase to form a Ni–Cu alloy.[13] The broad peak centered around 560 °C is attributed to the reduction of NiO to afford metallic Ni (Ni^0),[14] while the shoulder observed at higher temperatures (>700 °C) is attributed to $NiAl_2O_4$ reduction. Table S2 (ESI†) displays the surface concentration of elements detected by x-ray photoelectron spectroscopy (XPS) for E-NCA both as synthesized as well as reduced using conditions identical to those employed in the reactor before testing the catalyst in the conversion of BG to RD, *i.e.*, 350 °C for 3 hours under flowing H_2. The elements detected and their relative abundance were found to be Al $>$ O $> >$Ni $>$ Cu (not counting adventitious carbon). Tellingly, the surface concentration of Ni and Cu on the E-NCA catalyst shows that the Ni : Cu ratio increases from 3.7 for as synthesized E-NCA to 5.8 for reduced E-NCA, which suggests that some degree of metal redistribution takes place during reduction. The Ni 2p region of the x-ray photoelectron spectra for as synthesized and reduced E-NCA is shown in Fig. S4(a) in the ESI.† As synthesized E-NCA exhibits peaks assigned to Ni^0 and Ni^{2+} at binding energies (BE) of 854.50 eV and 855.22 eV, respectively. However, upon reduction, the Ni^0 peak shifts to a lower BE of 854.06 eV, while the Ni^{2+} peak shifts to 855.83 eV. Similarly, the Cu 2p region of the x-ray photoelectron spectra for as synthesized and reduced E-NCA is shown in Fig. S4(b) (ESI†). As synthesized E-NCA displays peaks assigned to Cu^0 and Cu^{2+} at a BE of 932.19 eV and 933.80 eV, respectively. Upon reduction, the Cu^0 peak shifts to a BE of 932.27 eV, consistent with previous reports on Ni–Cu catalysts.[15,16] All BE values are included in Table S3 (ESI†), which also includes information *vis-à-vis* the abundance of different Ni and Cu species and confirms that the fraction of Ni^0 and Cu^0 increases significantly after reduction.

The E-NCA catalyst (0.5 g) was mixed with the same amount of SiC (used as diluent) and reduced *in situ* at 350 °C for 3 hours under flowing H_2 (60 sccm; 40 bar) within a $\frac{1}{2}$ inch O. D. SS tubular fixed-bed reactor prior to being tested in the conversion of BG to RD. After reduction, the system temperature was adjusted to 325 °C before initiating a flow of 50 wt% BG in dodecane (used as solvent) at a rate of 0.02 mL min^{-1}, which corresponds to a weight hourly space velocity (WHSV) of 1 h^{-1} ignoring both diluent and solvent. Liquid products, which were collected using a gas–liquid separator placed downstream from the reactor and kept at 0 °C, were analysed using a dual detection GC method,[17] incondensable gases being collected using Tedlar® bags for GC analysis. The results of the analysis of the liquid products collected during an experiment lasting 300 h and performed in duplicate are included in Fig. 2(a). Notably, the E-NCA catalyst displayed quantitative (100%) BG conversion irrespective of time-on-stream (TOS). Also of note is the fact that the concentration of RD – defined as C10–C26 hydrocarbons per Neste, the main producer of RD worldwide[18] – was found to be $\gtrsim 93\%$ regardless of TOS. It should be noted that this value can be considered to be slightly underestimated, since it ignores any C12 produced (dodecane was quenched during GC analysis as it was the reaction solvent) as well as any C9 and C27 formed, which is relevant since some diesel definitions stipulate a broader carbon number range of C9–C27.[19,20] The remainder of
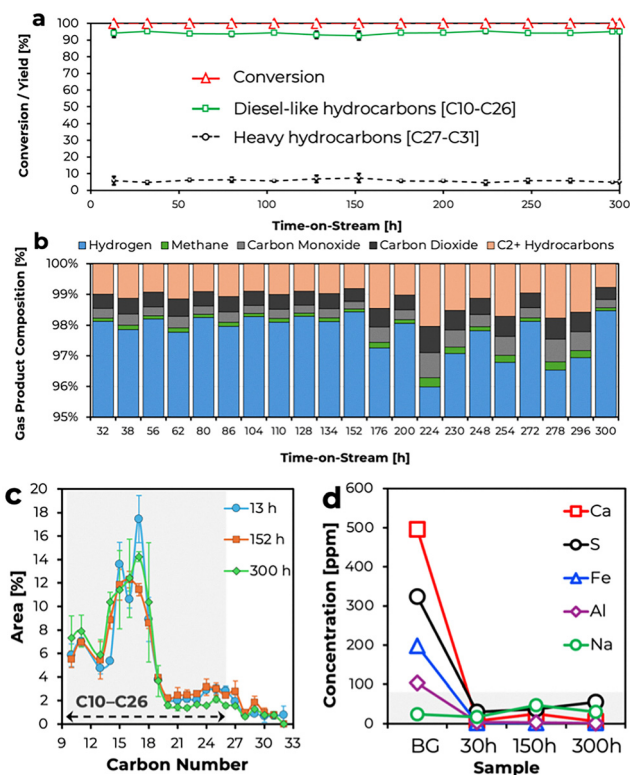
Fig. 2 Composition of (a) liquid and (b) gaseous products; (c) carbon number distribution of the liquid products; and (d) heteroatoms in the BG feed and representative liquid products.

the liquid products were found to be heavier (C27–C31) hydrocarbons, the concentration of which was found to be ⩽7% irrespective of TOS. Performing this experiment in duplicate allowed to assess both the repeatability and the statistical significance of the results, which were most satisfactory since standard deviations were calculated to be ±0.35 and ±2.62 for diesel-like (C10–C26) and heavy (C27–C31) hydrocarbons, respectively. A detailed breakdown of the carbon number distribution of liquid product samples representative of the beginning, middle, and end of these runs is shown in Fig. 2(c). Saliently, the majority (∼70%) of the products were found to be C17 or lighter hydrocarbons, which is unsurprising given that the BG sample utilized as feed is entirely composed of C18 and C16 fatty acids (see Table S1, ESI†) that would respectively afford C17 and C15 hydrocarbons upon decarboxylation/decarbonylation. Indeed, C17 and C15 hydrocarbons represent some of the most abundant products observed in Fig. 2(c) irrespective of TOS. Products heavier than C18 are likely the result of condensation reactions such as esterification and ketonization followed by deoxygenation and cracking,[8] which explains the low concentration of C27–C31 and C19–C31 hydrocarbons seen in Fig. 2(a) and (c).

Fig. 2(b) shows the composition of the incondensable gaseous reaction products as a function of TOS. The fact that the gaseous products contain both CO and CO_2 is consistent with fatty acid deoxygenation proceeding via decarbonylation and decarboxylation, respectively. The small amount of methane detected in the gaseous product stream is also noteworthy, since this

suggests that CO_x methanation is negligible, a welcome observation since methanation reactions consume considerable amounts of hydrogen and their occurrence would reduce the hydrogen efficiency of the process. However, the small amount of methane observed also indicates that the occurrence of cracking reactions resulting in the shortening of the alkyl chains through the loss of terminal carbons as methane is minimal. The latter is significant, since cracking over Ni–Cu/Al$_2$O$_3$ catalysts has been reported to mainly occur via the removal of terminal carbons in the form of methane when triglyceride-based feeds are employed.[21] Instead, the data in Fig. 2(b) suggests that the main cracking mechanism is the cleavage of C–C bonds more internal to the alkyl chain resulting in larger C2+ hydrocarbons in the gas phase, which is consistent with previously reported results dealing with the deoxygenation via deCO$_x$ of fatty acid-based feedstocks.[6,8] A more detailed breakdown of the C2+ gaseous products formed is provided in Fig. S5 (ESI†). In short, the C2+ gaseous products consist of similar amounts of ethane and propane along with smaller amounts of butane, propylene, and pentane in order of decreasing concentration, albeit traces of other unsaturated and/or branched C2–C5 hydrocarbons were also observed. Collectively considering the data pertaining to the liquid and gaseous products in Fig. 2(a)–(c), the concentration of heavy hydrocarbons in the liquid products and of light hydrocarbons in the gaseous products show an inverse relationship, which is to be expected since light gaseous hydrocarbons form at the expense of heavier liquid hydrocarbons.

The BG employed in this study as well as liquid product samples representative of the beginning, middle, and end of upgrading experiments were analyzed via ICP-MS to determine the concentration of contaminants of interest in both the feed and in the RD product mixtures as a function of TOS. Fig. 2(d) summarizes the results of these measurements, a more detailed accounting of the data acquired being provided in Table S4 (ESI†). The first thing worth noting is that the BG feed only contains significant amounts of Ca (496 ± 22.5 ppm), S (324.1 ± 20 ppm), Fe (198.1 ± 7.6 ppm), Al (103.7 ± 3.5 ppm) and Na (24.3 ± 4.3 ppm), the concentration of all other heteroatoms measured being below 10 ppm. Also of note is the fact that the concentration of these heteroatoms either remains low (as is the case of P, K, Mg, Si, N, Cu, Ni, and Pb) or is considerably reduced in the RD products relative to that in the feed (as is the case with Ca, S, Fe, and Al). The only exception to this is the case of Na, which is present in a similar concentration in the reaction products as it is in the BG feed. The negligible amount of Ni and Cu in the RD products irrespective of TOS indicates that the supported metals in the E-NCA catalyst do not leach into the reaction products under the reaction conditions employed and in the timeframe investigated. In short, most contaminants present in the feed are effectively removed during BG upgrading to afford a RD product stream relatively free of heteroatoms. Admittedly, sulfur is still present in concentrations above the 15 ppm maximum specified for some diesel grades; however, S concentration is well below the 500 or 5000 ppm maxima of other diesel grades.[22] It should also be noted that upgrading experiments were performed in the absence of a guard column, which is typically employed in industrial settings and would be expected to further reduce the heteroatom concentration in the RD product.

At the end of the BG upgrading experiments, the E-NCA catalyst was washed with hot dodecane and dried under flowing H_2 inside the reactor prior to taking samples from the top and bottom of the catalyst bed. The spent E-NCA catalyst samples recovered were subjected to thermogravimetric analysis (TGA) to ascertain the extent of fouling and/or coking. The results in Fig. S6(a) (ESI†) show a weight loss of ~17% and ~15% for the spent E-NCA catalyst sample taken from the top and bottom of the catalyst bed, respectively. The difference is consistent with the top of the catalyst bed interacting with the BG feed first, which provides more time for carbonaceous deposits to accumulate. In addition to their total amount, the nature of the carbonaceous deposits on the catalyst surface is also informative, the derivative curve in Fig. S6(b) (ESI†) including three distinct weight loss events. That observed between 200 and 450 °C, is attributable to the evaporation and combustion of reagents, products, and/or soft coke on the catalyst surface.[23] The weight loss between 450 and 650 °C can be attributed to hard coke, while a third weight loss above 650 °C is assigned to highly graphitic coke. Interestingly, the sample taken from the bottom of the catalyst bed displays higher amounts of hard and highly graphitic coke than that taken from the top. This may be due to the deposition of contaminants being more prevalent on the top of the catalyst bed (*vide infra*). Indeed, these contaminants could disrupt coke graphitization and/or serve as combustion catalysts during TGA. The spent E-NCA was also characterized *via* ICP-MS, XPS, and TEM-EDS. ICP-MS results (Table S5, ESI†) show that most contaminants present in BG (Table S4, ESI†) are present in the spent E-NCA, which explains their low concentration in the reaction products. XPS results provide information specific to the surface of samples taken from the top and the bottom of the catalyst bed (Table S6, ESI†). Tellingly, of the elements detected as contaminants in BG (see Table S4, ESI†) only P, S and Ca were also detected on the spent catalyst surface. Moreover, in contrast with the results in Tables S4 and S5 (ESI†) the relative concentration of these contaminants on the surface of spent E-NCA did not match their relative concentration in either BG or in the bulk of spent E-NCA. This suggest that these and other contaminants do not remain in the surface of the catalyst but diffuse into the bulk. Unsurprisingly, the concentration of the contaminants detected is higher on the surface of the spent E-NCA recovered from the top of the catalyst bed, since that part of the bed is exposed to the feed longer and acts as a guard for the material at the bottom of the catalyst bed. Lastly, TEM-EDS results reveal changes in metal particle size and composition that the catalyst undergoes during reaction. Fig. 1(a) shows that the metal particle size distribution shifts slightly towards larger particles during reaction, which is indicative of some degree of sintering. Fig. 1(d) illustrates that – relative to the fresh catalyst – spent E-NCA shows a much narrower Ni content of 55 to 70%, which approximates that expected from the composition of the bulk. It is worth noting that although contaminants accumulate on the catalyst surface and both the size and composition of supported metal particles change during the run, these changes do not perceptibly impact neither conversion nor selectivity, which remain stable throughout the run (see Fig. 2(a)).

In summary, an engineered NCA deCO$_x$ catalyst was synthesized, characterized, and tested in a continuous fixed-bed reactor to evaluate its performance and stability during the upgrading of BG (a waste FOG stream composed solely of free fatty acids) to RD for 300 h on stream. Results showed that BG conversion was quantitative and the yield of RD-like (C10–C26) hydrocarbons was excellent irrespective of TOS. Furthermore, the E-NCA catalyst effectively removed most heteroatoms in the BG feed to afford a RD product stream low in contaminants regardless of TOS. In addition, the E-NCA catalyst showed remarkable stability and resistance to deactivation caused by the leaching, sintering, or redistribution of metals, or by the fouling or coking of its surface. Therefore, this E-NCA deCO$_x$ catalyst – which represents a simple, inexpensive, active, selective, and stable formulation for the upgrading of waste FOG streams to fuel-like hydrocarbons – can be considered as the basis of a novel industrial process that can improve on the hydrotreating technology based on HDO over CoMo or NiMo formulations (see Table S7, ESI†) that is currently employed to effect this transformation.

Conflicts of interest

There are no conflicts to declare.

Data availability

Data supporting this article have been included as part of ESI.†

Notes and references

1 G. C. Umenweke and E. Santillan-Jimenez, *Hydrocarbon Biofuels*, American Chemical Society, 2024.
2 E. H. Cho, *et al.*, *Int. J. Hydrogen Energy*, 2017, **42**, 18350.
3 P. Bai, *et al.*, *Chem. Eng. J.*, 2024, **498**, 155220.
4 A. Srifa, *et al.*, *Bioresour. Technol.*, 2014, **158**, 81.
5 A. Srifa, *et al.*, *Chem. Eng. J.*, 2018, **345**, 107.
6 G. C. R. Silva, *et al.*, *Catalysts*, 2020, **10**(1), 91.
7 A. Kiméné, *et al.*, *J. Chem. Technol. Biotechnol.*, 2019, **94**(3), 658.
8 R. Loe, *et al.*, *Catalysts*, 2019, **9**, 123.
9 C. P. Ferraz, *et al.*, *Catal. Sci. Technol.*, 2021, **11**(9), 3025.
10 X. Chang, *et al.*, *J. Alloys Compd.*, 2023, **938**, 168557.
11 L. Zhao, *et al.*, *Catalysts*, 2023, **13**(8), 1190.
12 C. J. Breckner, *et al.*, *Chem. Phys. Chem.*, 2023, **24**(14), e202300244.
13 R. Loe, *et al.*, *Appl. Catal., B*, 2016, **191**, 147.
14 F. Wang, *et al.*, *Renewable Energy*, 2022, **195**, 1468.
15 G. C. Umenweke, *et al.*, *Fuel*, 2025, **392**, 134695.
16 J. Parker, *et al.*, *ChemNanoMat*, 2025, **11**(1), e202400222.
17 T. Morgan, *et al.*, *Energy Fuels*, 2017, **31**(9), 9498.
18 A. Engman, *et al.*, Neste Renewable Diesel Handbook, 2016.
19 Y. Kar, *et al.*, *Egypt. J. Pet.*, 2018, **27**(4), 1301.
20 A. Demirbas, *et al.*, *Pet. Sci. Technol.*, 2017, **35**(4), 406.
21 E. Santillan-Jimenez, *et al.*, *Catal. Today*, 2018, **302**, 261.
22 ASTM D975-21, https://www.astm.org/d0975-21.html.
23 H. Zhang, *et al.*, *Sci. Rep.*, 2016, **6**, 37513.